



# Dual templating fabrication of hierarchical porous three-dimensional ZnO/carbon nanocomposites for enhanced photocatalytic and photoelectrochemical activity



He Wang<sup>a</sup>, Xuan Liu<sup>b,\*</sup>, Shulan Wang<sup>a,\*</sup>, Li Li<sup>a,\*</sup>

<sup>a</sup> Department of Chemistry, School of Science, Northeastern University, Shenyang, 110819, China

<sup>b</sup> Department of Materials Science and Engineering, Carnegie Mellon University, Pittsburgh, PA, 15213, USA

## ARTICLE INFO

### Keywords:

ZnO  
Dual template  
Energy conversion  
Hierarchical pores

## ABSTRACT

Herein, a novel fabrication strategy to synthesize the ZnO/C nanocomposite with hierarchical porous structure was proposed with dual templating method that combines both ice and micelle templating. The composite material annealed at 900 °C showed the best photocatalytic reactivity for organic dye degradation compared with samples annealed at other temperatures, which is 2.2/7.0 times of the control ZnO + C sample under UV and visible light irradiation. The sample also showed superior photoelectrochemical performance while ultrasonic assisted photodegradation of methylene blue was also observed. This work demonstrates a novel and feasible approach for processing ZnO based photocatalysts with enhanced reactivity, which can be extended to the design of a broad series of functional metal oxide composites with high electrochemical performance for energy applications.

## 1. Introduction

Rapid economic development and population expansion serve as an efficient driving force to mitigate the environmental pollution and to alleviate the pressure arising from the energy crisis. Integration of energy materials and nanostructured devices is considered as an effective approach to solve the crisis [1,2]. Semiconductor photocatalysis and photoelectrochemical cell (PEC) have attracted significant attention as the potential sustainable and renewable technologies for solar energy harvesting and conversion to replace the conventional fossil fuel considering their applications in toxic organic pollutant degradation, CO<sub>2</sub> reduction, water splitting for hydrogen production, etc [3,4]. Among different metal oxide materials, ZnO is considered as one of the most important photocatalysts due to its physicochemical and functional advantages, such as non-toxicity, chemical stability, low expense, environmentally friendliness, etc. Meanwhile, ZnO has 10–100 times higher electron mobility than the commercial benchmark photocatalyst TiO<sub>2</sub>, which extends its applications into a broad range including piezoelectric devices, solar cell, catalysis, gas sensoring, etc [5–8]. Use of both mechanical vibration and solar energy [9] can increase the energy output of nanostructured devices such as nanogenerators [10,11] to capture energy from multiple power sources considering unpredictable and unstable availability of renewable energy sources. The special

piezoelectric output of ZnO with applied deformation also assists separation of photogenerated electrons and holes to different directions, resulting in decrease in their recombination rate, increase in photocatalytic efficiency and improvement in photocatalytic and photoelectrochemical performance [6–8].

As a multi-functional electronic semiconductor, ZnO has a wide band gap (3.37 eV). As a result, raw ZnO can only be activated under UV light irradiation with wavelength < 387 nm (4% of solar spectrum) [12]. To improve their photon absorption and to decrease the recombination rate of photo-generated charge carriers, different approaches have been attempted to increase their visible light response, such as metal and non-metal doping [13,14], dye sensitization [15,16] and oxide semiconductor coupling [17,18], etc. Recently, metal oxide/carbon mixture has attracted considerable attention to narrow down the band gap of metal oxide and to promote their quantum efficiency by intrinsic doping [13,19]. Furthermore, carbon can provide conductive channels for electrons to transfer after generation and also assist separation of photo-generated electron-hole pairs. For example, as one type of the high surface area carbon networks, graphene is widely used as the carbon source to couple with ZnO for the enhancement of its photo-activity [20–22]. ZnO in the small size (about 10 nm) dispersed on graphene showed excellent photocatalytic performance under UV light irradiation [23].

\* Corresponding authors.

E-mail addresses: [xuanliucmu@gmail.com](mailto:xuanliucmu@gmail.com) (X. Liu), [sliwang@mail.neu.edu.cn](mailto:sliwang@mail.neu.edu.cn) (S. Wang), [lilicmu@gmail.com](mailto:lilicmu@gmail.com), [lilicmu@alumni.cmu.edu](mailto:lilicmu@alumni.cmu.edu) (L. Li).

A hierarchical pore structure is important for practical applications of metal oxide and carbon materials in many fields, such as catalyst, gas adsorbent, energy storage, etc, considering the interconnected network between macropores and mesopores that can efficiently transport external species to the intrinsic active sites of component materials [24,25]. Particularly in photocatalytic applications, the macroporous channels can provide the light transfer path and extend the photon energy to reach the intrinsic surface of mesopores with enhancement in solar energy utilization efficiency and thus to increase photocatalytic activity [26,27]. Meanwhile, the macropores also can decrease the back-pressure during transportation of fluid and gas, and increase the flow rates of guest species within the hierarchical network.

Herein, we demonstrate a novel and simple strategy to synthesize a hierarchical ZnO/C porous structure by the dual templating method, combining ice templating alongside micelle-templating with citric acid-based zinc complexes as precursors. Different annealing temperatures on formation of pore structures as well as their photocatalytic activity for organic dye degradation were discussed in detail. Meanwhile, the ultrasonic-wave-generated piezo-phototronic effect of the synthesized ZnO for assisting photocatalytic reactivity and corresponding photoelectrochemical performance were also analyzed to further explore the use of materials for solar energy conversion. The advantage of current method is to provide a simple and feasible route for the fabrication of ZnO/carbon with micro-, meso-, and macro-porous structures together into the nanocomposites. Meanwhile, this method is also broadly applicable to the fabrication of other metal oxide/carbon materials, such as TiO<sub>2</sub>, SnO<sub>2</sub>, et al., which significantly extends its use to a wide range of energy and electronic related applications. To the best of our knowledge, this is the first report about dual templating method to fabricate hierarchical porous 3D ZnO/carbon nanocomposites at three different length scales for enhanced photocatalytic and photoelectrochemical activity.

## 2. Experimental

### 2.1. Sample preparation

Zn(CH<sub>3</sub>COO)<sub>2</sub>·2H<sub>2</sub>O (AR 99%, Aladdin, Shanghai) was used as the zinc precursor while pluronic F127 (EO<sub>106</sub>PO<sub>70</sub>EO<sub>106</sub>) copolymer (Sigma, St. Louis, MO, USA) served as the soft template for mesoporous structure and carbon sources. In the synthesis of ZnO/C composite materials, 70 mg F127 and 437.3 mg Zn(CH<sub>3</sub>COO)<sub>2</sub>·2H<sub>2</sub>O were dissolved in a mixture of deionized water (5 mL) and ethanol (5 mL) by ultrasonic followed with addition of 144 mg of citric acid (AR 99%, TianJin, Yongda). The solution was then under continuous ultrasonic to form milky suspension. The solution was transferred to a 25 mL plastic tube and plunged into liquid nitrogen bath for 30 min to fully freeze the samples, followed with freeze drying for 24 h to remove the ice template by sublimation. The white powders were calcined for 1 h at 250 °C and then heated to different temperatures in the range from 400 °C to 1000 °C with a heating rate of 10 °C/min for 30 min to form the hierarchical ZnO/C framework. In addition, commercial ZnO was mechanically mixed with sucrose and annealed at 900 °C (noted ZnO + C(900 °C)) as the control sample, while the mixture without annealing was used as another reference.

### 2.2. Structural characterization

X-Ray diffraction (XRD) patterns were obtained on a Ultima IV (Rigaku, Japan) with CuK $\alpha$  radiation ( $\lambda = 0.1542$  nm) at the working voltage of 40 kV and current of 40 mA. Surface morphology and elemental analysis was investigated by field-emission scanning electron microscope (SEM) (Ultra Plus, Carl Zeiss, Germany) equipped with energy dispersive spectroscopy (EDS). X-ray photoelectron spectroscopy (XPS) measurement was conducted to examine chemical bonding between ZnO and carbon on ESCALAB 250Xi (Thermo Fisher Scientific)

analyzer with Al Ka ( $\hbar\nu = 1486.6$  eV) as the excitation source. Room-temperature Raman spectroscopy was measured by Finder Vista at 532 nm with 10% filter. High resolution transmission electron microscopy (TEM) was conducted using a Tecnai G2 F20 S-TWIN at an acceleration voltage of 200 kV. Nitrogen adsorption/desorption isotherms (American Micromeritics ASAP 2020 sorptometer) were obtained at 77 K to determine the specific surface area of the samples using the Brunauer-Emmett-Teller (BET) analysis method while pore size distribution was obtained by the Barret-Joyner-Halenda (BJH) model based on the desorption data and pore volume measured at  $P/P_0 = 0.99$  point. Thermogravimetric and differential thermal analyses (TG/DTA) (METTLER TOLEDO-3) were used to analyze the ZnO precursor at 25–1100 °C with a heating rate of 10 °C/min under nitrogen atmosphere with a flow rate of 100 mL/min.

### 2.3. Photocatalytic dye degradation setup

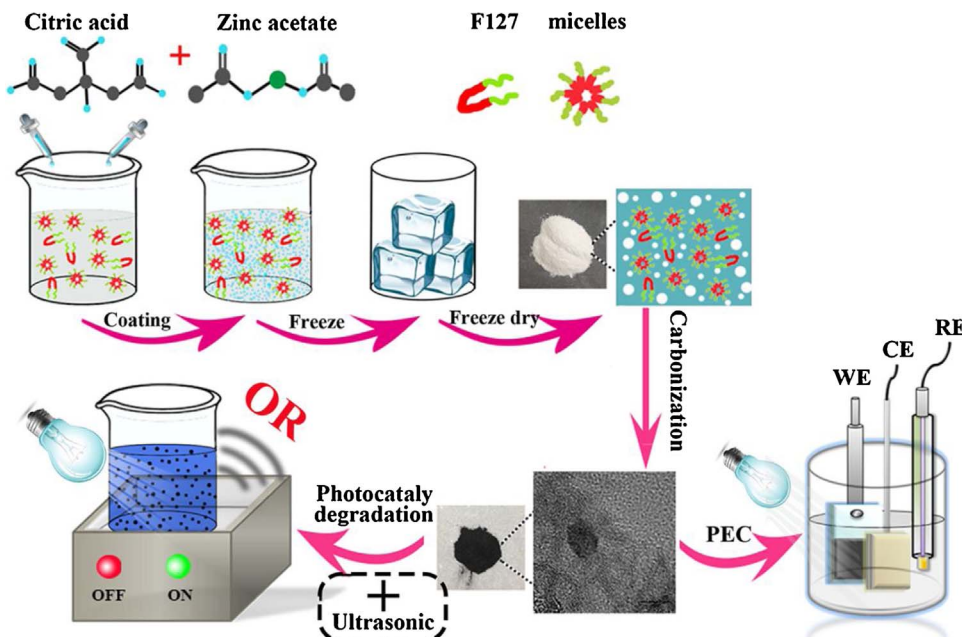
The photocatalytic methylene blue (MB, Shenyang Chemical Reagent Co. Ltd., P.R. China.) degradation with ZnO/C was measured under UV and visible light produced from 125 W high-pressure mercury lamp and 300 W high-pressure xenon lamp with a 420 nm cutoff filter (PLS-SXE 300), respectively. The light intensities used for the photocatalytic experiments are 250 mW/cm<sup>2</sup> (visible) and 310 mW/cm<sup>2</sup> (UV). 15 mg ZnO/C photocatalyst was added into 80 mL  $4 \times 10^{-5}$  M MB solution under magnetic stirring for 60 min in dark to reach the adsorption-desorption equilibrium before photocatalytic reaction. 6 mL solution was taken out in certain duration intervals during illumination and centrifuged to remove the catalyst for further analysis. Degradation of MB was then evaluated with a UV-vis spectrophotometer by comparing the intensity of the maximum absorbance peak ( $\lambda = 664$  nm) (denoted as C) and the initial intensity (denoted as C<sub>0</sub>) before irradiation. To investigate the ultrasonic-wave-generated piezo-phototronic effect of the ZnO/C nanocomposites, an ultrasonic probe with the frequency of 50 kHz was placed into the suspensions to provide mechanical vibration.

### 2.4. Photoelectrochemical (PEC) measurements

$2 \times 1$  cm FTO glass was cleaned by acetone, ethyl alcohol and water successively before photoelectrochemical measurement. ZnO/C (900 °C) powder was then mixed with N-methyl pyrrolidone solution to form the slurry which was then uniformly coated onto the surface of FTO substrate and dried at 80 °C. The electrochemical measurements were then carried out with a three-electrode photoelectrochemical cell in 1 M Na<sub>2</sub>SO<sub>4</sub> aqueous electrolyte with ZnO/C coated FTO glass as the working electrode, Pt as the counter electrode and a saturated calomel electrode (SCE) as the reference. Linear sweep voltammetry was swept linearly from 0 to 1.2 V vs SCE at a scan rate of 50 mV s<sup>-1</sup>. The photocurrent measurement was performed in the visible range by using a 300 W high-pressure xenon lamp with the 420 nm cutoff filter. Detailed experimental setup for material synthesis and photocatalytic/photoelectrochemical performance evaluation is shown in Scheme 1.

## 3. Results and discussion

The phase composition of ZnO/C samples was investigated with XRD and the results are shown in Fig. 1a and b. The samples annealed at 600–900 °C exhibit the characteristic peaks corresponding to the (100), (002), (101), (102), (110), (103), (200), (112) and (201) planes, which are consistent with the reference peaks from hexagonal wurtzite ZnO (JCPDS-36-1451). No other phases relating to impurities are observed in the patterns. With increase in the annealing temperatures over 600 °C, the sharp narrow peaks with high diffraction intensity are formed, confirming the improvement of crystallization for samples. The corresponding crystallite size was also calculated by Scherrer's equation and shown in Table 1. Based on the results, it can be observed that the



**Scheme 1.** The synthetic flow of hierarchical porous ZnO/C nanocomposites and the corresponding photochemical characterization.

crystallite size increases with increase in annealing temperatures. Note that the characteristic peaks of ZnO are significantly weakened when temperature reaches 1000 °C, which is attributed to reduction of ZnO at the temperature over 950 °C [28]. Fig. 1b shows the enlarged diffraction patterns of (100), (002) and (101) planes that are shifted to lower angles compare with pure ZnO with increase in the annealing temperature, which is attributed to deformation of the ZnO lattice induced by carbon doping. All samples showed larger lattice parameters than the commercial ZnO, confirming the substitution of O atom by C can expand the lattice cell and increase the volume considering the oxygen atoms have small radius (O: 60 pm; C: 70 pm) [29–31]. The samples annealed at 900 °C shows the largest lattice expansion compared with samples annealed at other temperatures. Meanwhile, note that the lattice parameter expansion is not huge, which demonstrates the carbon doping is limited in some degree and increasing temperatures lead to the slightly increase of doping levels.

The Raman spectra of ZnO/C samples annealed at different temperatures is performed to investigate the structure of carbons, as shown in Fig. 1c. Two distinct peaks at 1346 cm<sup>-1</sup> and 1594 cm<sup>-1</sup> are assigned to D and G bands of carbon, which are attributed to stretching and breathing of sp<sup>2</sup> and sp<sup>3</sup> atoms in rings, respectively. Similarly to the previous report, no other characteristic peaks at the lower Raman shift are observed for the current case [32]. The G band is evidenced as representative of nanocrystalline carbon and the sp<sup>2</sup>-hybridized carbon

**Table 1**

The lattice parameters, cell volume and crystallite size of ZnO/C compositions at different temperature.

Temperature (°C)	Lattice constants			V <sub>cell</sub> (Å <sup>3</sup> )	Crystallite size (nm)
	a (Å)	b (Å)	c (Å)		
600	3.25016	3.25016	5.20735	47.63	15.39
700	3.25032	3.25032	5.20761	47.65	26.3
800	3.25257	3.25257	5.20904	47.73	52.59
900	3.25394	3.25394	5.20998	47.77	55.98
ZnO	3.250	3.250	5.207	47.6	–

atoms caused by the carbonization for ordered carbon while the D band is an indication of less disordered carbon with six carbonic rings [33]. In the current case, the I<sub>D</sub>/I<sub>G</sub> value of ZnO/C decreased with the calcination temperatures, demonstrating the increased graphitization degree which is beneficial for improvement in electronic conductivity of samples.

Fig. 2a shows TG/DTA curves of the ZnO/C sample at a heating rate of 10 °C min<sup>-1</sup> under nitrogen flow. Three steps of weight loss were observed for ZnO precursor with the first step weight loss occurring between 95 °C and 300 °C. The corresponding weight loss is attributed to evaporation of absorbed water and small organic molecules that arises from F127 addition and the other organic component in ZnO/C

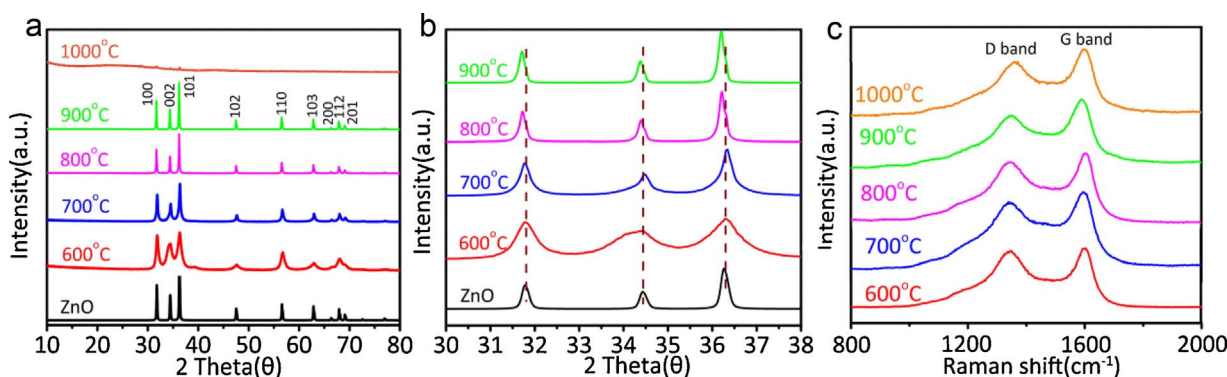


**Fig. 1.** (a) XRD patterns of ZnO/C at different temperatures from 600 to 1000 °C. The commercial pristine ZnO was also used as the reference; (b) the enlarged region of XRD patterns between 30° and 38°; (c) Raman spectrum of the as-prepared ZnO/C annealed at different temperatures.

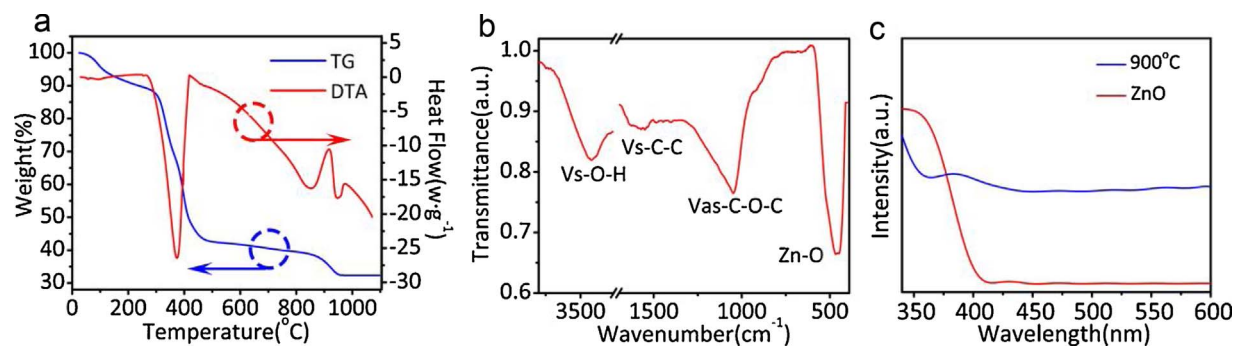


Fig. 2. (a) TG/DTA curves of ZnO precursor after ice templating treatment; (b) FT-IR spectra of ZnO/C at 900 °C; (c) Diffuse reflectance spectra of ZnO and ZnO/C annealed at 900 °C.

nanocomposites. The approximate 45% mass loss between 300 °C and 450 °C is related to decomposition of zinc compounds for ZnO formation. The mild weight loss between 910 and 950 °C is due to reduction in ZnO with produced carbon, which is consistent with the previous report [28]. The final weight loss also explains why less crystalline phase is observed for samples annealed at 1000 °C.

The surface group of ZnO/C annealed at 900 °C was analyzed with FTIR, and the results are shown in Fig. 2b. The peak at 3430 cm<sup>-1</sup> is related to the stretching vibration of O–H that is attributed to water adsorption on the surface of the samples [34]. The weak shoulder peaks at 1609–1564 cm<sup>-1</sup> correspond to the stretching vibration band of C–C, while the band at 1051 cm<sup>-1</sup> is the asymmetric stretching peak of C–O–C. The peaks at above 450 cm<sup>-1</sup> belong to characteristic peaks of Zn–O [35,36]. To investigate the photon absorption of the samples, UV-vis diffuse reflectance spectra of ZnO/C at different temperatures as well as pure commercial ZnO are presented in Fig. 2c (with all other samples shown in Fig. S1). Different from pristine ZnO, the ZnO/C samples extended the absorption spectrum from the UV region to visible light with narrowed band gap.

To probe the surface composition and chemical interaction between ZnO and carbon, XPS was performed on ZnO/C sample annealed at 900 °C between 0 and 1200 eV, as shown in Fig. 3. Based on the survey spectra, only Zn, C, and O were detected while no other impurity elements are observed. The Zn 2p (Fig. 3b) spectra shows two

characteristic peaks at 1022.7 eV and 1045.4 eV that are assigned to the binding energy of Zn 2p<sub>3/2</sub> and Zn 2p<sub>1/2</sub>, respectively, confirming formation of ZnO in the composites [37,38]. The asymmetric wide peak in the O 1s spectrum indicates existence of multi-chemical states, as shown in Fig. 3d. The O 1s peak at 531 eV corresponds to the Zn–O bond at the wurtzite structure of hexagonal ZnO, while the higher binding energy peak at 532.8 eV is attributed to formation of the C–O bond [39,40]. The C 1s XPS spectrum can be divided into two peaks that are related to the peak of C–C and C–O at the binding energy of 284.4 eV and 286 eV, which are attributed to delocalized alternant hydrocarbon and carbon doping into the ZnO lattice by hybridization of O 2p and C 2p orbitals [12,41,42]. The atomic percentages (as shown in Table S3) are similar for the samples annealed from 600 to 900 °C, which are around 15%, 18%, 67% for Zn, C, and O, respectively. However, the carbon content increased greatly to 92% for the samples annealed at 1000 °C. This is consistent with the XRD result which confirms that ZnO is partially converted to Zn following with the evaporation of Zn under the annealing temperature of 1000 °C.

Surface morphology and microstructure of the ZnO/C composite annealed at 900 °C was investigated by scanning electron microscopy (SEM) at different magnifications, as shown in Fig. 4a and b. The long range disordered macropores with diameters in the range of 0.1–0.5 μm can be clearly observed. Many large-sized mesopores can also be seen in Fig. 4c and d. The sidewall of the macropores is composed with

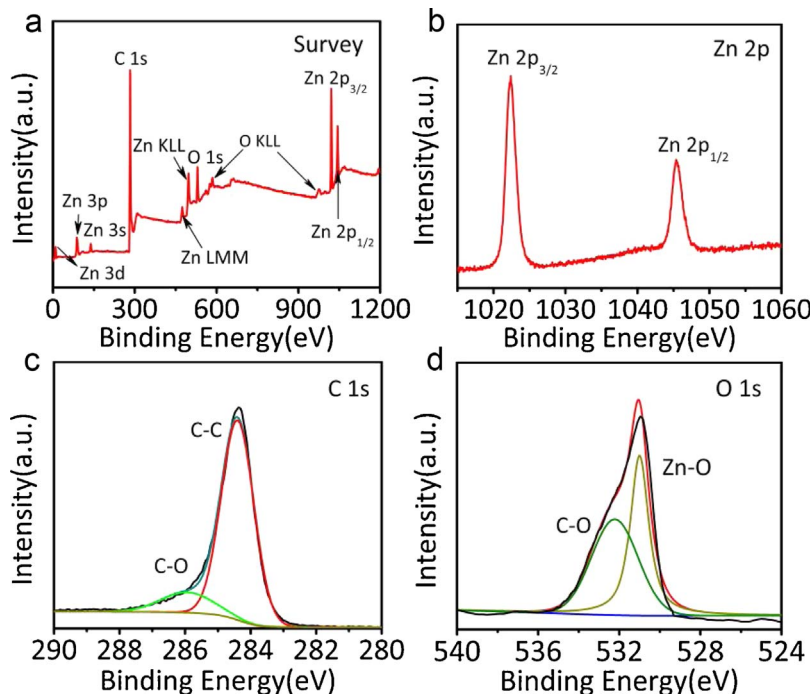
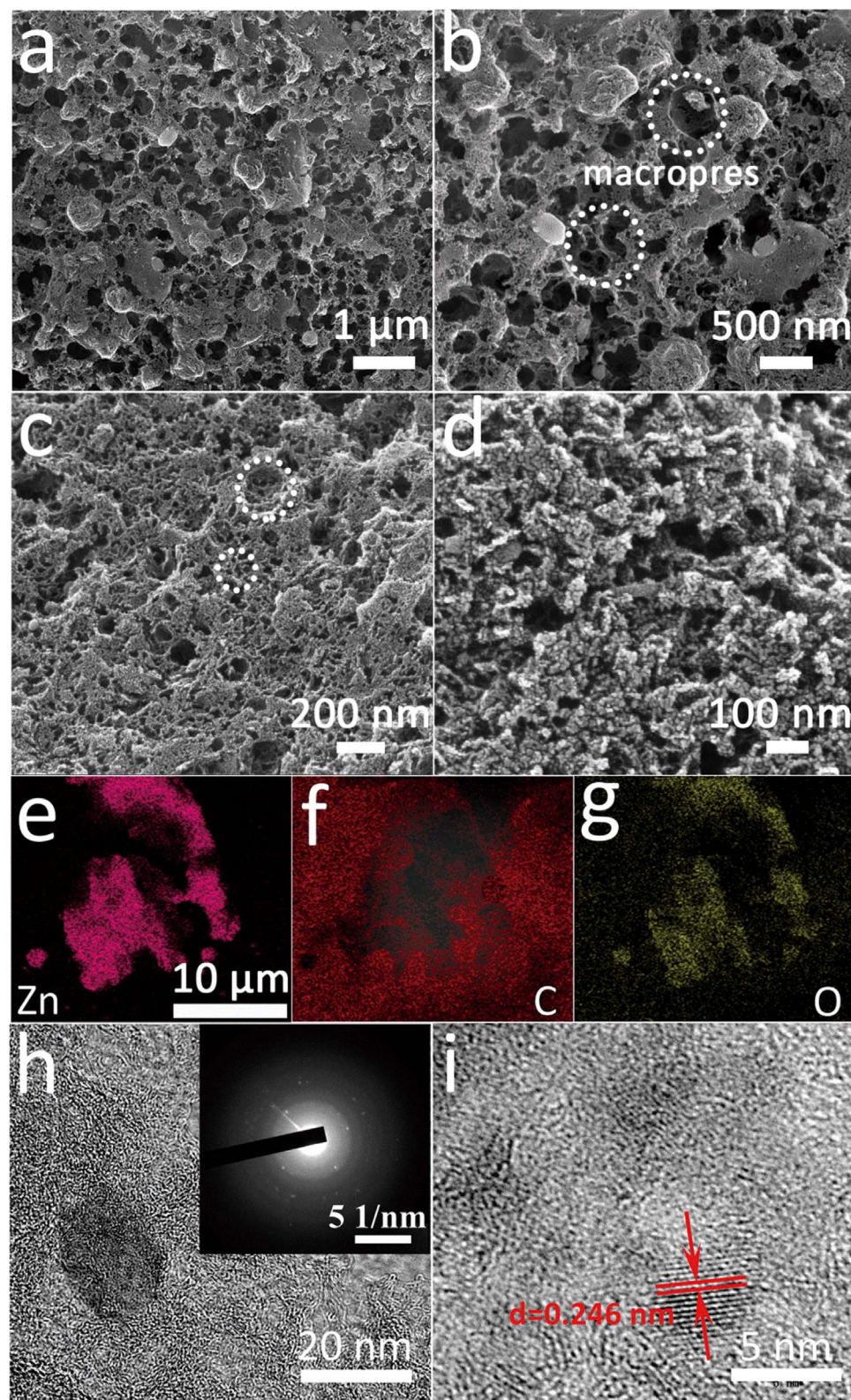


Fig. 3. XPS of (a) survey spectra, (b) Zn 2p, (c) C 1s and (d) O 1s for ZnO/C annealed at 900 °C.



**Fig. 4.** (a,b,c,d) SEM images of ZnO/C nanocomposites annealed at 900 °C with low and high magnifications; (e-g) EDX mapping of the ZnO/C composite after etching; (h) TEM bright field image of ZnO/C with the selected area electron diffraction (SAED) pattern as the inset; and (i) high resolution TEM to show the lattice fringe of ZnO/C.

interconnected mesopores formed between small nanoparticles. ZnO/C nanocomposites annealed at lower temperatures were also measured with the SEM images shown in Fig. S2. Based on SEM images, all the ZnO/C nanocomposites showed the clear macropores within the structures while the increasing temperature is beneficial for the formation of macropores. The increased macropores can ensure the fast flow rates within the hierarchical porous structure and more photons

also can get access to ZnO for efficient absorption. Detailed energy dispersive X-ray (EDX) element mapping is used to evaluate distribution of Zn, C and O in the matrix of ZnO/C nanocomposite and the results are shown in Fig. 4e–g. Based on the result, it can be observed that ZnO is surrounded by carbon, which can provide the electron transfer channel during the photocatalytic reaction through their interfacial chemical bonding that is confirmed by XPS result. The microstructure

**Table 2**

Surface area and pore structure information of ZnO/C at different annealed temperatures.

Samples	$S_{\text{BET}}$ ( $\text{m}^2 \text{g}^{-1}$ )	$S_{\text{micro}}$ ( $\text{m}^2 \text{g}^{-1}$ )	$S_{\text{meso}}$ ( $\text{m}^2 \text{g}^{-1}$ )	$V_{\text{pore}}$ ( $\text{m}^3 \text{g}^{-1}$ )	$V_{\text{micro}}$ ( $\text{m}^3 \text{g}^{-1}$ )	$V_{\text{meso}}$ ( $\text{m}^3 \text{g}^{-1}$ )
400 °C	29.6	6.2	23.73	0.109	0.007	0.097
500 °C	57.7	3.53	41.4	0.155	0.001	0.141
600 °C	61.7	3.6	56.7	0.167	0.0015	0.155
700 °C	67	4.2	63.8	0.171	0.0012	0.165
800 °C	89.5	10.7	75.1	0.201	0.001	0.192
900 °C	112.1	11.2	89.1	0.345	0.003	0.307

$S_{\text{micro}}$  and  $S_{\text{meso}}$  are the surface areas of the micropores and mesopores, respectively;  $V_{\text{pore}}$  is the total pore volume;  $V_{\text{micro}}$  and  $V_{\text{meso}}$  are the volumes of the micropores and mesopores, respectively.

and morphology of the ZnO/C composites were further investigated with TEM bright field images as shown in Fig. 4h. ZnO was dispersed into the carbon matrix uniformly and can be distinguished based on the contrast. The selected area electron diffraction (SAED) pattern in the inset with crystalline rings confirms the polycrystalline nature of ZnO that is consistent with the hexagonal wurtzite structures. In the high-resolution transmission electron microscopy (HRTEM) image of the ZnO crystalline, the lattice space is measured to be 0.246 nm, which corresponds to the (002) plane of the wurtzite structure (Fig. 4i).

The surface area and pore structure information of ZnO/C annealed at different temperatures are shown in Table 2 and the  $N_2$  adsorption-desorption isotherms as well as pore size distribution is shown in Fig. 5. Different from conventional understanding that increase in the annealing temperature leads to decrease in the surface area due to coarsening of nanoparticles, the BET surface area of ZnO/C nanocomposites in the current case increased from 400 °C to 900 °C. Meanwhile, it can be clearly noticed that the crystallite size confirmed by XRD also increased with the annealing temperature. We suspect this trend is attributed to the increased surface area of mesopores which makes a major contribution to the total surface area of the ZnO nanocomposites. High annealing temperatures lead to complete evaporation of the micelle template and formation of a larger number of mesopores. A similar trend has been observed in the fabrication of ZnO by calcining pre-synthesized ZIF-8 polyhedra [43]. In addition, all samples show a type IV  $N_2$  adsorption-desorption isothermal with the hysteresis loops that confirm the mesoporosity of the samples. Note that even at high temperatures like 900 °C, the nanocomposites still maintain the robust pore structure without evidence of pore collapse. The outstanding thermal stability is important for fabrication of high performance carbon based nanocomposites since a necessarily high annealing temperature is required to keep high conductivity of carbon. With a further increase in the annealing temperature to 1000 °C, the surface area of nanocomposites exhibits a dramatic increase for both the total surface area and the mesoporous portion (as shown in Table S1 and Fig. S3). This increase is attributed to conversion of ZnO to Zn at approximately 950 °C for evaporation while the primary component in the nanocomposite is carbon, as confirmed by XRD and TG results shown in Figs. 1 and 2. Combined with clear observation of macroporous formation in the SEM images in Fig. 4, the hierarchical interconnected porous structure of ZnO/C at three different levels (micro-, meso-, macro-) is formed successfully with combination of the dual templating method. In contrast, the control sample ZnO + C mechanical mixture annealed at 900 °C showed much smaller surface area (as shown in Fig. S3 and Table S1), which confirms the dual templating method proposed in the current work is a very effective strategy to fabricate ZnO/C nanocomposites with unique hierarchical pore structures and thus can provide abundant active sites for the photochemical reactions.

Methylene blue (MB) solution is used as the organic dye to evaluate the photocatalytic reactivity of ZnO/C nanocomposites under UV and visible light irradiation at different annealing temperatures and the result is shown in Fig. 6a and b. Adsorption equilibrium is reached

before the photocatalytic reactions. The characteristic absorption peak of MB at 664 nm was selected to monitor the photocatalytic degradation process at different time intervals [44], with the ZnO/C annealed at 900 °C as an example to illustrate photocatalytic characterization shown in Fig. S4. Degradation of MB with all samples followed the pseudo-first-order reaction as shown below in Eq. (1):

$$\ln\left(\frac{C}{C_0}\right) = kt \quad (1)$$

where  $C_0$  is the original concentration of MB,  $C$  the concentration of MB at time  $t$ ,  $k$  the reaction rate constant ( $\text{min}^{-1}$ ), and  $t$  the irradiation time (min). The linear relationship between the degradation of MB by ZnO/C nanocomposites and reaction time are plotted in Fig. 6c and d. The commercial ZnO, ZnO and C mechanical mixture as well as the corresponding annealing sample were used as the control sample with increase in the annealing temperature, the photocatalytic reactivity of ZnO/C nanocomposites under UV and visible irradiation are both enhanced and the sample calcined at 900 °C shows the best reactivity with  $k$  values of 0.22 and 0.03  $\text{min}^{-1}$ , respectively, which are 2.2 and 7.0 times  $k$  values of the ZnO + C mechanical mixture annealed at the same temperatures. Self-degradation of MB under exposure (denoted as "MB") is confirmed by the data shown in Fig. 6a and b while the reactivity is very low and can be negligible. Further annealing of ZnO/C sample leads to degradation of ZnO to Zn, resulting in a significant decrease in the photocatalytic reactivity. Stability issue is considered as one of the most apparent drawbacks that limits the use of semiconductor powders for photocatalytic applications and lead to the decrease of the photoreactivity [45]. Different approaches have been used to improve the photostability of ZnO based photocatalysts, such as surface hybridization of ZnO with  $C_{60}$ , carbon nanotube or graphene [19,45,46]. The recycled photocatalytic activity of ZnO/C nanocomposites calcined at 900 °C was also analyzed under both UV and visible light irradiation, respectively, with the result shown in Fig. 6e and f. Based on the figure, it can be noticed that the prepared sample did not show apparent decrease of the photocatalytic reactivity for methylene blue degradation even after 4 cycles, indicating the porous ZnO/carbon nanocomposites prepared in the current work have the excellent photostability under exposure.

As a piezoelectric semiconductor material, ZnO has shown mechanical-assisted electrical field formation which may promote separation of photogenerated charge carriers and improve the photocatalytic reactivity [47,48]. To validate this assumption, ultrasonic wave was introduced into the reaction system to create an internal electric field within ZnO. Corresponding results with and without the ultraosonic wave under visible light irradiation are shown in Fig. 6g. It can be clearly observed that the same ZnO/C sample under ultrasonic wave showed improved photocatalytic reactivity compared with the samples without addition of ultrasonic wave. The photoelectrochemical response of ZnO/C and the control mechanical mixture of ZnO + C annealed at 900 °C were investigated and the photocurrent density-potential (J-V) curves ranging from 0 to 1.2 V vs SCE under visible light exposure are presented in Fig. 6h with the open circuit curves as the inset. Based on the Linear Sweeps Voltammogram (LSV) result showed in the figure, it can be observed that the control ZnO + C mechanical mixtures exhibited poor photocurrent density. On the contrast, the as-prepared ZnO/C sample showed tremendous improvement in the photocurrent performance—1.5  $\text{mA cm}^{-2}$  at the potential of 0.99 V [1.23 V vs reversible hydrogen electrode (RHE)]. Under illumination, the photo-generated holes transport through the ZnO/C/electrolyte interface for water oxidation while electrons move through FTO to reach the counter Pt electrode for reduction, as illustrated in Fig. 7b. The unique pore structure as well as robust interfacial bonding between ZnO and carbon contributes to the high photoelectrochemical performance of the sample. The photocurrent density of the ZnO/C sample showed a gradually increased trend with the applied potential at an onset

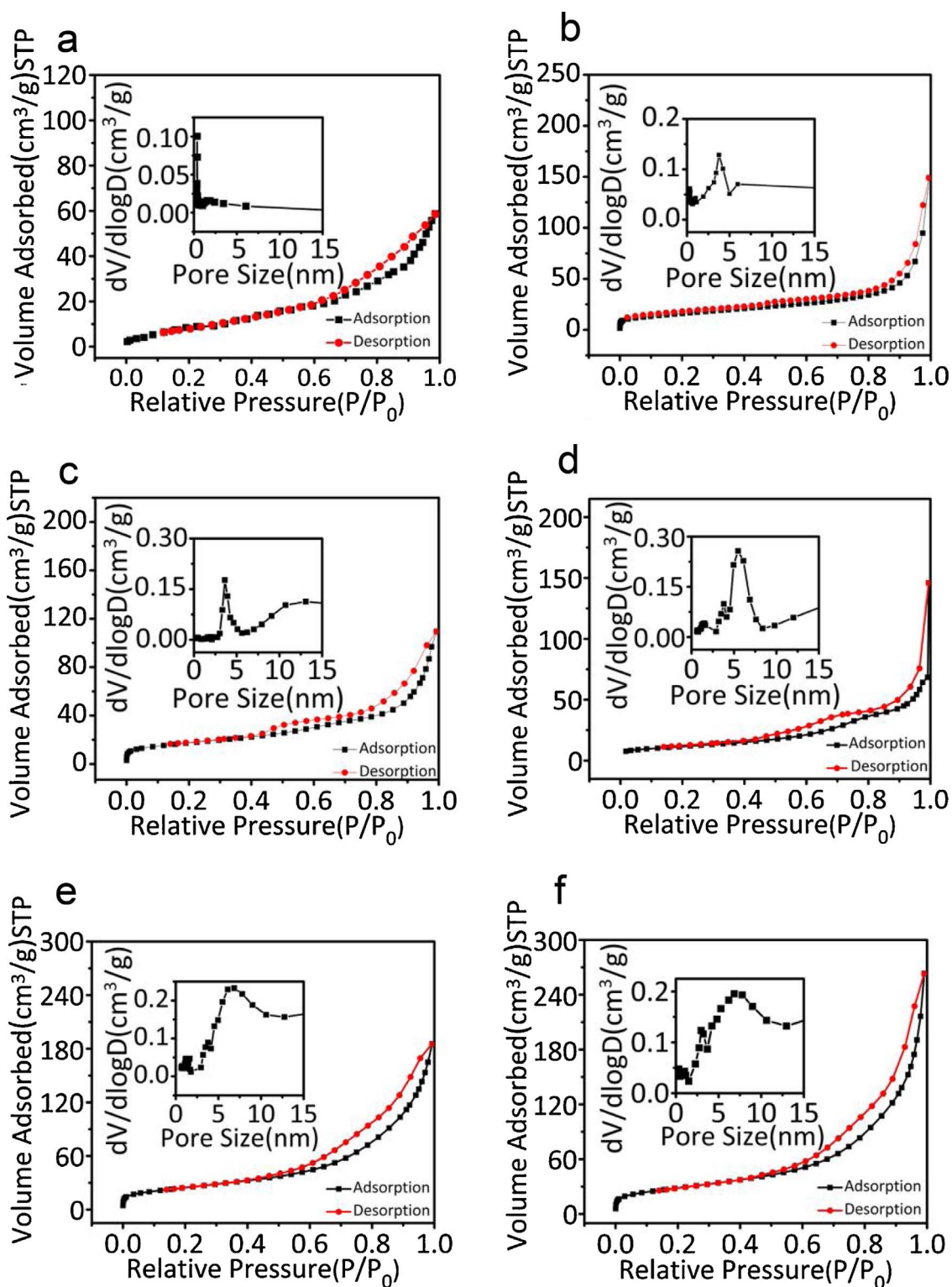


**Fig. 5.**  $N_2$  adsorption-desorption isotherms of ZnO/C nanocomposites annealed at different temperatures: (a) 400 °C, (b) 500 °C, (c) 600 °C, (d) 700 °C, (e) 800 °C and (f) 900 °C; the inset shows the pore size distribution derived from Barrett-Joyer-Halenda (BJH) method.

potential of  $-0.02$  V vs SCE. The low photocurrent onset ( $-0.02$  V in the current case) is crucial for the improvement of the photoelectrochemical performance since the applied potential bias to reach the maximum photocurrent is reduced and the overall efficiency of PEC is therefore increased [49].

Herein, a dual templating method combining F127 serving as the soft micelle template and ice-templation was used to fabricate the

three-dimensional hierarchical porous structure at three different scale levels (micro-, meso-, macro-) and the photocatalytic activity as well as the photoelectrochemical activity of the samples annealed at different temperatures are discussed. We attribute the enhanced photocatalytic activity of ZnO/C nanocomposites shown in the current work to their unique hierarchical pore structure, strong interfacial bonding between carbon and photoactive materials, and the effective inter-doping

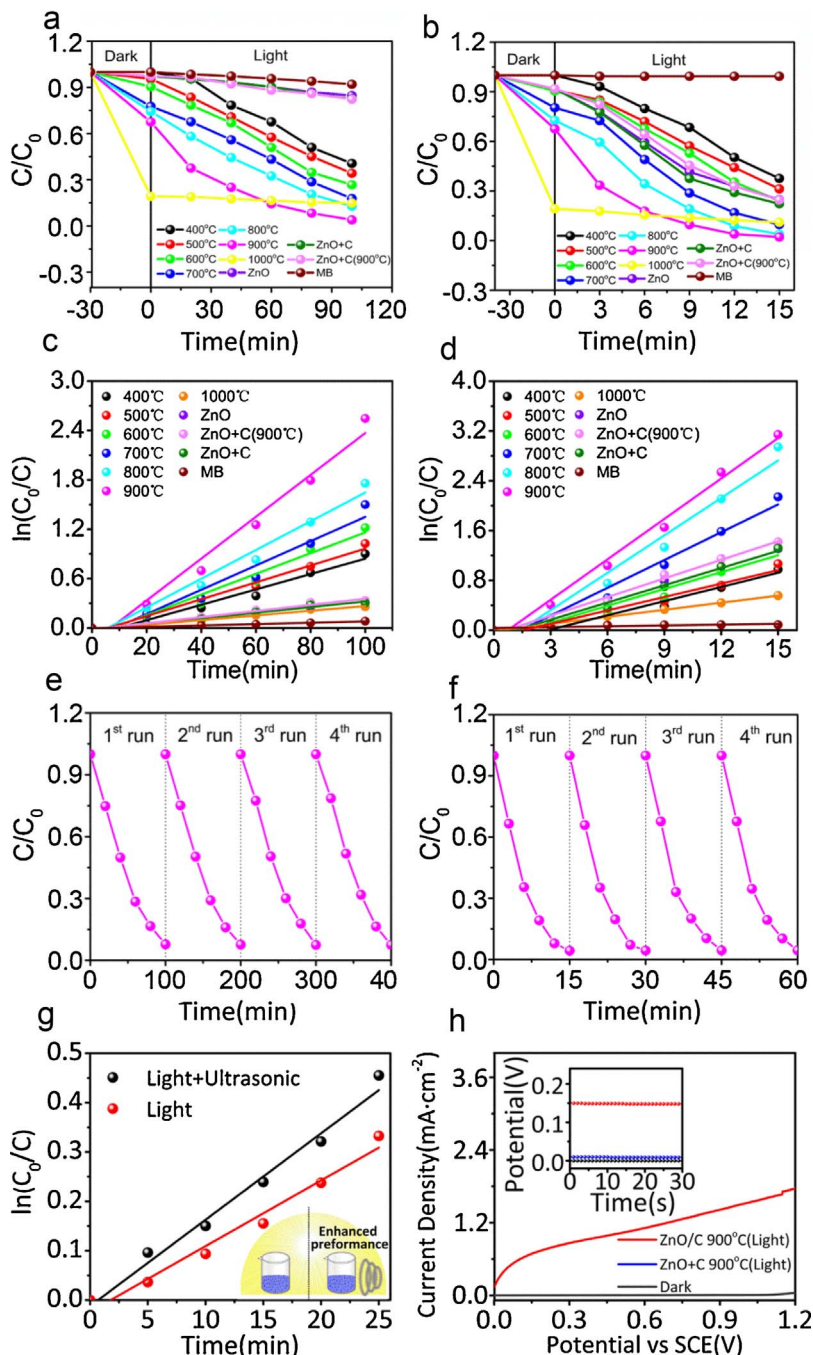


**Fig. 6.** Photoactivity of ZnO/C annealed at different temperatures for MB degradation under visible and UV light irradiation: (a), (b) adsorption and degradation; (c), (d) logarithm of MB concentration against time; (e), (f) stability study for samples annealed at 900 °C; (g) ultrasonic assisted degradation of samples annealed 900 °C; (h) photocurrent -potential curves annealed at 900 °C under visible light irradiation. “Dark” is related to the sample without light exposures. The inset is the corresponding open circuit curves.

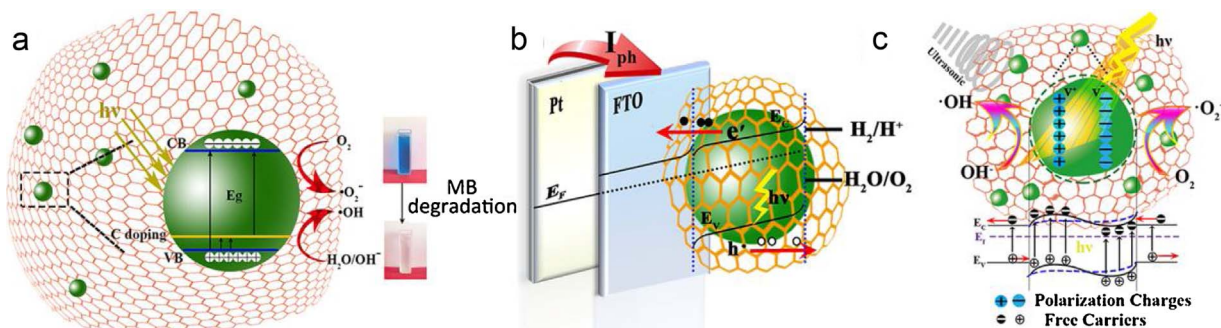


**Fig. 7.** Schematic illustration of (a) the photocatalytic mechanism of ZnO/C to degrade methylene blue; (b) transfer path of electrons and holes within the PEC system; and (c) the piezophotocatalytic process for ZnO/C under ultrasonic wave and illumination.

(Fig. 7a). This novel interconnected hierarchical pore structure can enhance inter-reflection of absorbed light within the semiconductor powders and thus increase the light-absorption efficiency [2]. In addition, the sufficient surface area is beneficial for complete penetration of reagent solutions into internal surfaces and decreases the transferring path of the electrons and holes, while the surface area can be adjusted by the carbon loading content that is not extended for discussion in the current work. Nevertheless, an apparent advantage of this method that needs to be noted is to prepare the ZnO/C nanocomposites with larger surface area when compared with the control samples including nanocomposites without ice templation and mechanical mixture. Other than the electrical matrix for electron transfer, carbon also dopes into ZnO for increasing the visible light absorption of the samples by narrowing the band gap [19,50]. Ice templating is crucial for the formation of macroporous structure and photoactivity enhancement of the nanocomposites. As shown in Fig. S5, the values of K for organic dye degradation with ice templation were about 1.71 (UV) and 1.86 (visible) times of the sample without the treatment of ice templation while keeping all the other treatment conditions are the same. This confirms that the use of ice templating shown in the current work is in great necessity for the enhancement of photocatalytic activity.

The annealing temperature is crucial for formation of the pore structures and determination of the reactivity of samples. Different from conventional observations, the elevated temperatures did not degrade the total surface area due to degradation of micelle templates and formation of increased number of mesopores, although the crystallite size of ZnO increased with the annealing temperature. Furthermore, as shown in Table 2, more mesopores are formed with enhanced annealing temperatures, which are responsible for the effective surface area of samples as well as establishment of the stable interface between the solution and photocatalytic compounds. Note that even at the highest allowable temperatures of 900 °C, the pore structure still showed excellent thermal stability without collapse of the pore structure. Enhanced reactivity of ZnO/C nanocomposites annealed at 900 °C compared with other temperatures is attributed to multiple microstructure based parameters, including surface area, formation of hierarchical pore structures, crystallinity and carbon graphitization degree, etc. In the current case, ZnO/C nanocomposites annealed at 900 °C showed high surface area ( $112 \text{ m}^2 \text{ g}^{-1}$ ) and percentage of mesopores (79.5%), high crystallinity of ZnO, and great graphitization degree ( $I_D/I_G = 0.861$ ), all of which contributed to its excellent photoactivity. In addition, its effective carbon doping level and hierarchical pore structures also ensure the efficient photogenerated charge carrier transfer within the nanostructures [51].

Another interesting phenomenon shown in the current work is the piezoelectric assisted photo-reactivity induced by the external ultrasonic wave [52,53]. Currently, the primary barrier for the low efficiency of photocatalysis is the recombination of the photogenerated charge carriers and the back reaction of intermediates [54–59]. Introduction of the effective internal or external electric field can move the electrons and holes in the photoactive components to the different directions and thus increase their reactivities for water splitting or organic dye degradation. Our group has proposed the use of ferroelectric polarization [60,61], surface termination [62] and p-n junctions [60] to introduce the internal electrical field. Herein, the mechanical piezoelectric confirmed the enhanced photocatalytic and photoelectrochemical activity of the ZnO/C samples compared with the control samples, which is consistent with the previous reports [10,11]. The induced electric field can increase the width of space charge region and also the height of the surface band bending, which lead to the increased driving force for separation of photo-generated charge carriers. Considering the nanoscaled ZnO with a very small particle size, its band bending cannot be fully related to the bulk levels. In the current state, both negative (the induced polarization direction points into ZnO) and positive (opposite direction) polarization exist with the band bending for charging the surface to form either accumulation or depletion

layers. The width of the accumulation and depletion layers are dependent on the surface potential  $V_s$  and Debye length  $L_D$  [58,63]:

$$L_d = \left( \frac{2eV_s}{kT} \right)^{1/2} L_D \quad (2)$$

$$L_a = \sqrt{2} \left( 1 - \exp \left[ \frac{eV_s}{2kT} \right] \right) L_D \quad (3)$$

where  $L_d$  and  $L_a$  are the width of depletion layer and accumulation layer, e the electron charge, k the Boltzmann constant (in units of eV/K), and T the absolute temperature. The surface potential is determined by the surface polarization while Debye length in the current case is considered to show a negligible change. The addition of the piezoelectric polarization thus can lead to the increased width of accumulation and depletion layers. These interfacial charges can also have partial contribution from the surface charge of local chemical state variation, though the piezoelectric charge is expected to be much larger than that from the local chemical variation [56]. The simplified mechanism can be found in Fig. 7c as the illustration.

#### 4. Conclusions

In the current work, ZnO/C nanocomposites with a three-dimension hierarchical pore structure at three different levels (micro-, meso-, macro-) was successfully synthesized via a novel and feasible dual templating method that combines both ice and micelle-templation following with the pyrolysis for carbonation. The ZnO/C samples showed the superior UV and visible photocatalytic reactivity for MB degradation at the temperature of 900 °C, which is 2.2 and 7.0 times of the control ZnO/C samples, respectively. In addition, the sample also shows the excellent photoelectrochemical performance with the photocurrent density of  $1.5 \text{ mA cm}^{-2}$  at the potential of 0.99 V, while the control sample showed a negligible photocurrent density. The ultrasonic induced piezoelectric is confirmed to increase the photocatalytic activity of the samples by assisting the separation of photogenerated electrons and holes. This direct and feasible fabrication strategy provides an effective route to synthesize the ZnO based carbon nanocomposites with the hierarchical pore structures and can be extended to a broad range of metal oxide systems with high performance for the potential application of photocatalysis and other energy conversion/storage devices.

#### Acknowledgement

This work was supported by the National Natural Science Foundation of China (51574062, 51274058).

#### Appendix A. Supplementary data

Supplementary data associated with this article can be found, in the online version, at <http://dx.doi.org/10.1016/j.apcatb.2017.10.012>.

#### References

- [1] J. Lee, H.S. Lim, Y.S. Kang, K.D. Suh, RSC Adv. 5 (2015) 104556–104562.
- [2] D. Ding, W. Lan, Z. Yang, X. Zhao, Y. Chen, J. Wang, X. Zhang, Y. Zhang, Q. Su, E. Xie, Mater. Sci. Semicond. Process. 47 (2016) 25–31.
- [3] D. Ding, K. Liu, S. He, C. Gao, Y. Yin, Nano Lett. 14 (2014) 6731–6736.
- [4] S. Kuriakose, B. Satpathi, S. Mohapatra, Phys. Chem. Chem. Phys. 16 (2014) 12741–12749.
- [5] H.M. Chen, C.K. Chen, Y.C. Chang, C.W. Tsai, R.S. Liu, S.F. Hu, W.S. Chang, K.H. Chen, Angew. Chem. Int. Ed. Engl. 49 (2010) 5966–5969.
- [6] S.K. Kansal, M. Singh, D. Sud, J. Hazard. Mater. 141 (2007) 581–590.
- [7] M. Muruganandham, I.S. Chen, J.J. Wu, J. Hazard. Mater. 172 (2009) 700–706.
- [8] S.G. Ullattil, P. Periyat, B. Naufal, M.A. Lazar, Ind. Eng. Chem. Res. 55 (2016) 6413–6421.
- [9] C.F. Tan, W.L. Ong, G.W. Ho, ACS Nano 9 (2015) 7661–7670.
- [10] Z.L. Wang, J.H. Song, Science 312 (2006) 242–246.
- [11] F.R. Fan, Z.Q. Tian, Z.L. Wang, Nano Energy 1 (2012) 328–334.
- [12] F. Wang, L. Liang, L. Shi, M. Liu, J. Sun, Dalton Trans. 43 (2014) 16441–16449.
- [13] D. Zhang, J. Gong, J. Ma, G. Han, Z. Tong, Dalton Trans. 42 (2013) 16556–16561.

[14] Y.P. Zhu, M. Li, Y.L. Liu, T.Z. Ren, Z.Y. Yuan, *J. Phys. Chem. C* 118 (2014) 10963–10971.

[15] Z. Dong, X. Lai, J.E. Halpert, N. Yang, L. Yi, J. Zhai, D. Wang, Z. Tang, L. Jiang, *Adv. Mater.* 24 (2012) 1046–1049.

[16] J. Jiang, X. Zhang, P. Sun, L. Zhang, *J. Phys. Chem. C* 115 (2011) 20555–20564.

[17] V. Jeena, R.S. Robinson, *Chem. Commun.* 48 (2012) 299–301.

[18] S. Balachandran, M. Swaminathan, *Dalton Trans.* 42 (2013) 5338–5347.

[19] C. Han, M.Q. Yang, B. Weng, Y.J. Xu, *Phys. Chem. Chem. Phys.* 16 (2014) 16891–16903.

[20] Q. Zhang, C. Tian, A. Wu, T. Tan, L. Sun, L. Wang, H. Fu, *J. Mater. Chem.* 22 (2012) 11778–11784.

[21] Y.T. Kwon, S.O. Kang, J.A. Cheon, Y. Song, J.J. Lee, Y.H. Choa, *Appl. Surf. Sci.* 415 (2017) 2–7.

[22] M. Darwish, A. Mohammadi, N. Assi, Q.S. Manuchehri, Y. Alahmad, S. Abuzerr, *J. Alloys. Compd.* 703 (2017) 396–406.

[23] R.K. Upadhyay, N. Soin, S.S. Roy, *RSC Adv.* 4 (2014) 3823–3851.

[24] Y. Qin, F. Zhang, Y. Chen, Y. Zhou, J. Li, A. Zhu, Y. Luo, Y. Tian, J. Yang, *J. Phys. Chem. C* 116 (2012) 11994–12000.

[25] K. Naito, T. Tachikawa, M. Fujitsuka, T. Majima, *J. Am. Chem. Soc.* 131 (2009) 934–936.

[26] X. Chen, X. Wang, X. Fu, *Energy Environ. Sci.* 2 (2009) 872.

[27] N. Linares, A.M. Silvestre-Albero, E. Serrano, J. Silvestre-Albero, J. Garcia-Martinez, *Chem. Soc. Rev.* 43 (2014) 7681–7717.

[28] Y. Li, Z. Liu, H. Liu, B. Peng, *J. Clean. Prod.* 143 (2017) 311–318.

[29] E. Hasabeldaim, O.M. Ntwaeborwa, R.E. Kroon, E. Coetsee, H.C. Swart, *Opt. Mater.* (2017) 1–11.

[30] X. Zhou, Y. Li, T. Peng, W. Xie, X. Zhao, *Mater. Lett.* 63 (2009) 1747–1749.

[31] O. Bechambi, S. Sayadi, W. Najjar, *J. Ind. Eng. Chem.* 32 (2015) 201–210.

[32] S. Xie, X. Lu, T. Zhai, W. Li, M. Yu, C. Liang, Y. Tong, *J. Mater. Chem.* 22 (2012) 14272–14275.

[33] C. Castiglioni, F. Negri, M. Rigolio, G. Zerbi, *J. Chem. Phys.* 115 (2001) 3769–3778.

[34] Y. Zhao, L. Liu, T. Cui, G. Tong, W. Wu, *Appl. Surf. Sci.* 412 (2017) 58–68.

[35] Z. Xing, Y. Chen, C. Liu, J. Yang, J. Xu, Y. Situ, H. Huang, *J. Alloys Compd.* 708 (2017) 853–861.

[36] X. Bai, C. Sun, D. Liu, X. Luo, D. Li, J. Wang, N. Wang, X. Chang, R. Zong, Y. Zhu, *Appl. Catal. B: Environ.* 204 (2017) 11–20.

[37] M. Ahmad, E. Ahmed, Z.L. Hong, N.R. Khalid, W. Ahmed, A. Elhissi, *J. Alloys Compd.* 577 (2013) 717–727.

[38] C. Luo, D. Li, W. Wu, C. Yu, W. Li, C. Pan, *Appl. Catal. B: Environ.* 166–167 (2015) 217–223.

[39] J. Liu, X. Li, L. Dai, *Adv. Mater.* 18 (2006) 1740–1744.

[40] M. Zhou, X. Gao, Y. Hu, J. Chen, X. Hu, *Appl. Catal. B: Environ.* 138–139 (2013) 1–8.

[41] S.T. Kochuveedu, Y.H. Jang, Y.J. Jang, D.H. Kim, *J. Mater. Chem. A* 1 (2013) 898–905.

[42] X. Liu, H. Du, X.W. Sun, B. Liu, D. Zhao, H. Sun, *CrystEngComm* 14 (2012) 2886.

[43] S. Liu, J. Wang, J. Yu, *RSC Adv.* 6 (2016) 59998–60006.

[44] J. Sun, H. Fan, N. Wang, S. Ai, *Sep. Purif. Technol.* 160 (2016) 67–72.

[45] Y. Zhang, Z. Chen, S. Liu, Y.-J. Xu, *Appl. Catal. B: Environ.* 140–141 (2013) 598–607.

[46] H. Fu, T. Xu, S. Zhu, Y. Zhu, *Environ. Sci. Technol.* 42 (2008) 8064–8069.

[47] Y. Zhang, C. Liu, J. Liu, J. Xiong, J. Liu, K. Zhang, Y. Liu, M. Peng, A. Yu, A. Zhang, Y. Zhang, Z. Wang, J. Zhai, Z.L. Wang, *ACS Appl. Mater. Interfaces* 8 (2016) 1381–1387.

[48] K.Y. Lee, B. Kumar, J.S. Seo, K.H. Kim, J.I. Sohn, S.N. Cha, D. Choi, Z.L. Wang, S.W. Kim, *Nano Lett.* 12 (2012) 1959–1964.

[49] G. Wang, H. Wang, Y. Ling, Y. Tang, X. Yang, R.C. Fitzmorris, C. Wang, J.Z. Zhang, Y. Li, *Nano Lett.* 11 (2011) 3026–3033.

[50] J. Mu, C. Shao, Z. Guo, Z. Zhang, M. Zhang, P. Zhang, B. Chen, Y. Liu, *ACS Appl. Mater. Interfaces* 3 (2011) 590–596.

[51] X. Zhang, J. Qin, R. Hao, L. Wang, X. Shen, R. Yu, S. Limpanart, M. Ma, R. Liu, J. *Phys. Chem. C* 119 (2015) 20544–20554.

[52] J. Shi, M.B. Starr, H. Xiang, Y. Hara, M.A. Anderson, J.H. Seo, Z. Ma, X. Wang, *Nano Lett.* 11 (2011) 5587–5593.

[53] W. Yang, Y. Yu, M.B. Starr, X. Yin, Z. Li, A. Kvist, S. Wang, P. Zhao, X. Wang, *Nano Lett.* 15 (2015) 7574–7580.

[54] L. Li, X. Liu, Y. Zhang, P.A. Salvador, G.S. Rohrer, *Int. J. Hydrogen Energy* 38 (2013) 6948–6959.

[55] L. Li, Y. Zhang, A.M. Schultz, X. Liu, P.A. Salvador, G.S. Rohrer, *Catal. Sci. Technol.* 2 (2012) 1945–1952.

[56] L. Li, G.S. Rohrer, P.A. Salvador, E. Dickey, *J. Am. Ceram. Soc.* 95 (2012) 1414–1420.

[57] N.V. Burbure, P.A. Salvador, G.S. Rohrer, *Chem. Mater.* 22 (2010) 5831–5837.

[58] A. Bhardwaj, N.V. Burbure, A. Gamalski, G.S. Rohrer, *Chem. Mater.* 22 (2010) 3527–3534.

[59] H. Li, Y. Sang, S. Chang, X. Huang, Y. Zhang, R. Yang, H. Jiang, H. Liu, Z.L. Wang, *Nano Lett.* 15 (2015) 2372–2379.

[60] L. Li, X. Liu, Y. Zhang, N.T. Nuhfer, K. Barmak, P.A. Salvador, G.S. Rohrer, *ACS Appl. Mater. Interfaces* 5 (2013) 5064–5071.

[61] L. Li, P.A. Salvador, G.S. Rohrer, *Nanoscale* 6 (2014) 24–42.

[62] J.L. Giocondi, G.S. Rohrer, *J. Am. Ceram. Soc.* 86 (2003) 1182–1189.

[63] W. Monch, Springer (2004) 147–160.